Solar Phys
DOI 10.1007/s11207-014-0610-y

Observational Signatures of Waves and Flows in the Solar Corona

I. De Moortel · P. Antolin · T. Van Doorsselaere

Received: 12 July 2014 / Accepted: 8 October 2014

Abstract Propagating perturbations have been observed in extended coronal loop structures for a number of years, but the interpretation in terms of slow (propagating) magneto-acoustic waves and/or as quasi-periodic upflows remains unresolved. We used forward-modelling to construct observational signatures associated with a simple slow magneto-acoustic wave or periodic flow model. Observational signatures were computed for the 171 Å Fe IX and the 193 Å Fe XII spectral lines. Although there are many differences between the flow and wave models, we did not find any clear, robust observational characteristics that can be used in isolation (*i.e.* that do not rely on a comparison between the models). For the waves model, a relatively rapid change of the average line widths as a function of (shallow) line-of-sight angles was found, whereas the ratio of the line width amplitudes to the Doppler velocity amplitudes is relatively high for the flow model. The most robust observational signature found is that the ratio of the mean to the amplitudes of the Doppler velocity is always higher than one for the flow model. This ratio is substantially higher for flows than for waves, and for the flows model used in the study is exactly the same in the 171 Å Fe IX and the 193 Å Fe XII spectral lines. However, these potential observational signatures need to be treated cautiously because they are likely to be model-dependent.

Keywords Flows · Magnetohydrodynamics (MHD) · Sun: corona · Waves

I. De Moortel (✉)
School of Mathematics and Statistics, University of St. Andrews, St. Andrews, Fife, KY16 9SS, UK
e-mail: ineke.demoortel@st-andrews.ac.uk

P. Antolin
National Astronomical Observatory of Japan, 2-21-1 Osawa, Mitaka, Tokyo 181-8588, Japan
e-mail: patrick.antolin@nao.ac.jp

T. Van Doorsselaere
Centre for Mathematical Plasma Astrophysics, Mathematics Department, KU Leuven, Celestijnenlaan 200B bus 2400, 3001 Leuven, Belgium
e-mail: tom.vandoorsselaere@wis.kuleuven.be

Published online: 31 October 2014

1. Introduction

Since the advent of high-resolution imagers, many observations of intensity (density) perturbations travelling along coronal loops have been made. From the very outset, however, two different interpretations of these propagating coronal disturbances (PCDs) were found in the literature: a propagating, slow magneto-acoustic wave and periodic upflows can both lead to periodic density perturbations, which would be observed as propagating, periodic intensity variations by imaging instruments. For a comprehensive review of these propagating (coronal) disturbances, we refer for example to De Moortel (2009), De Moortel and Nakariakov (2012), or Banerjee, Gupta, and Teriaca (2011).

Initial reports by Schrijver *et al.* (1999) and Winebarger *et al.* (2002) found lower propagation speeds (of about 40 $\mathrm{km\,s^{-1}}$), and hence supported an interpretation in terms of a (quasi-) periodic flow model. Subsequently, however, various authors reported similar disturbances in coronal plumes (*e.g.* Ofman *et al.*, 1997; DeForest and Gurman, 1998; Banerjee, O'Shea, and Doyle, 2000) and large coronal (fan) loops at the edges of active regions (*e.g.* Berghmans and Clette, 1999; De Moortel, Ireland, and Walsh, 2000; De Moortel *et al.*, 2002a, 2002b), propagating at speeds close to the local sound speed, which led to an alternative interpretation in terms of slow magneto-acoustic waves. Combined with theoretical modelling, which explained the decay of the perturbations in terms of thermal conduction (*e.g.* Ofman, Nakariakov, and Sehgal, 2000; De Moortel and Hood, 2003, 2004), the slow wave model became widely accepted. More recently, however, additional spectral observations provided by the *Hinode*/EUV Imaging Spectrometer (EIS; Culhane *et al.*, 2007) have reopened the debate on whether to interpret the observed PCDs as a slow propagating wave or as quasi-periodic upflows. Not only are perturbations in intensity observed, but also in other parameters such as Doppler velocity, line-widths, and red-blue asymmetries, which appear consistent with an interpretation in terms of quasi-periodic upflows (*e.g.* Sakao *et al.*, 2007; Doschek *et al.*, 2008; Del Zanna, 2008; Hara *et al.*, 2008; Harra *et al.*, 2008; McIntosh and De Pontieu, 2009a, 2009b; De Pontieu *et al.*, 2009, 2011; De Pontieu and McIntosh, 2010; He *et al.*, 2010; Bryans, Young, and Doschek, 2010; Tian, McIntosh, and De Pontieu, 2011; Ugarte-Urra and Warren, 2011; Warren *et al.*, 2011). Again we refer to De Moortel and Nakariakov (2012) as well as to McIntosh (2012) for a more thorough review of the literature.

Following this new series of observations, however, Verwichte *et al.* (2010) and Wang, Ofman, and Davila (2012) pointed out that it would still be possible to interpret the combined imagining and spectral observations in terms of slow magneto-acoustic waves, which leaves the interpretation of the observed PCDs inconclusive. We also refer to Peter (2010) for a discussion on the observed asymmetries in EUV emission lines. Both the slow wave and the periodic upflow models can partially explain the observations, but neither can currently account for all of the observed properties. This is perhaps most clearly illustrated by Wang *et al.* (2009) and De Pontieu and McIntosh (2010), who analysed exactly the same dataset, but arrived at a different interpretation, with the first explaining the observed PCDs in terms of slow magneto-acoustic waves and the latter using a quasi-periodic upflow model. More recently, a dual model has been suggested, where quasi-periodic flows at the very footpoints of the loops generate a slow magneto-acoustic wave that travels further along the loops (at the local sound speed), as *e.g.* in the observations of Nishizuka and Hara (2011) or the model of Ofman, Wang, and Davila (2012) and Wang, Ofman, and Davila (2013).

Although the debate might seem a mainly semantic one, there are important underlying physical implications. If the observed PCDs are indeed propagating slow magneto-acoustic waves, seismology can be used to derive local plasma parameters. Using this interpretation,

for example, Marsh, Walsh, and Plunkett (2009) and Marsh and Walsh (2009) inferred the local plasma temperature and Van Doorsselaere *et al.* (2011) estimated the local thermal conduction coefficient and polytropic index. If, on the other had, the PCDs are indeed quasi-periodic upflows, they could play a significant role in the coronal mass cycle given their abundant and continuous presence in large coronal loops and fans (see *e.g.* McIntosh and De Pontieu, 2009b; McIntosh *et al.*, 2010, 2012; De Pontieu *et al.*, 2011).

As the observational data have been pushed to their (current) limits, we here take a different approach to try and resolve this debate. We use theoretical modelling of both a propagating slow magneto-acoustic wave and a periodic flow combined with forward-modelling to study the possible observational signatures of each model (see *e.g.* De Moortel and Bradshaw, 2008; Owen, De Moortel, and Hood, 2009; Antolin and Van Doorsselaere, 2013). The model setup and forward-modelling process are described in more detail in Section 2, followed by a description of the initial-value Fe IX results (Section 3), the Fe IX results for a harmonic driver (Section 4), and the results for the Fe XII line (Section 5). A discussion of the results and conclusions are presented in Sections 6 and 7.

2. Model Setup and Forward-Modelling

To determine observationally distinguishable signatures for propagating waves and periodic flows, we constructed a simple, 2D numerical model using LareXd (Arber *et al.*, 2001). The uniform, background medium has a typical coronal temperature of $T_0 = 1$ MK and density of $n_0 = 10^{15}$ m^{-3}. A propagating (longitudinal) wave is modelled by using a lower-boundary driver of the form

$$v(x, y = 0, t) = A \sin(\omega_{\text{wave}} t),$$

whereas a flow is modelled by

$$v(x, y = 0, t) = A \sin^2(\omega_{\text{flow}} t).$$

Here A is the amplitude and ω is the frequency. Small amplitudes are used to avoid non-linear interactions. Note that because

$$\sin^2 \omega = \frac{1}{2}(1 - \cos 2\omega), \tag{1}$$

we use $\omega_{\text{flow}} = \omega_{\text{wave}}/2$, where $\omega_{\text{wave}} = 2\pi$ (corresponding to a period of 300 s in dimensional units), to obtain perturbations with the same frequency (see Figure 1). However, this

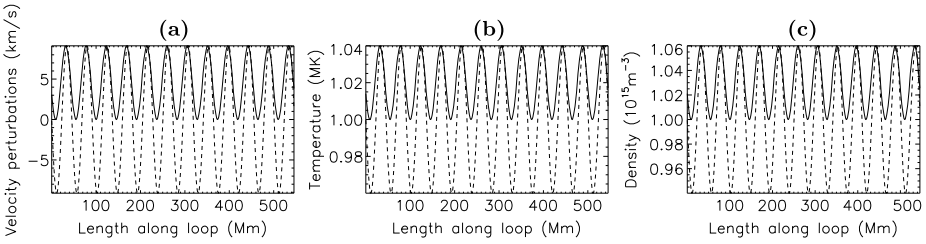

Figure 1 Evolution of the (a) velocity, (b) temperature, and (c) density as a function of distance along the loop for the flow (solid lines) and wave (dashed lines) models.

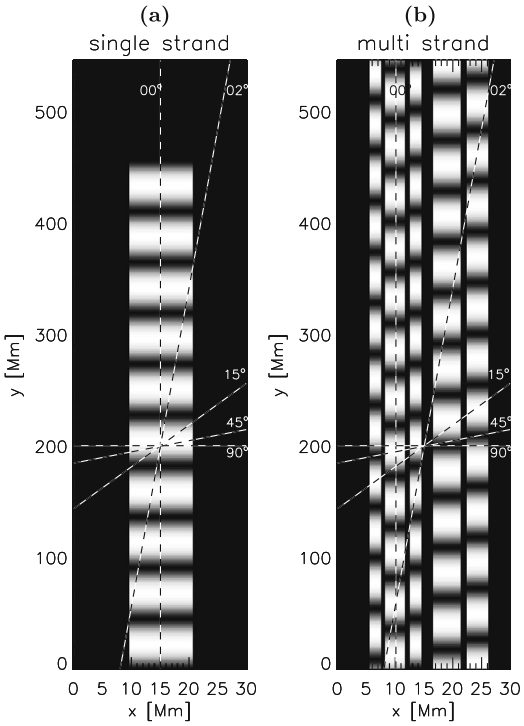

Figure 2 Snapshots showing (a) the initial-value single-strand (at $t = 3000$ s) and (b) the steady-state multistrand perturbations and the rays used to trace at different angles (dashed lines).

immediately tells us that the periodic flow can be decomposed into a (periodic) wave and a steady background flow with the same amplitude. The boundary-driven velocity perturbations travel along the loop at the local sound speed (for both the wave and flow perturbations), generating associated temperature and density perturbations. As can be seen from Figure 1, the perturbations associated with the wave mode (dashed lines) oscillate around the equilibrium values, whereas the flow perturbations are always greater than the background values. In this sense, there is already little physical difference between the wave and flow simulations because the periodic flow simulation is just a propagating sound wave on top of a background flow. From our simulations, we found no evidence of periodic flows that would propagate at a speed slower than the sound speed, nor any indication of how they could be initiated. The periodic inflow at the footpoint automatically triggers an upwardly propagating sound wave.

Two different versions of the model were created. The first is a simple, single strand of perturbations embedded in a uniform background as shown in Figure 2(a). The second model represents a multistrand loop, consisting of five small sections of perturbations all with the same periods, but slightly out of phase, as shown in Figure 2(b).

Observational signatures were subsequently forward modelled, using the forward-modelling code[1] FoMo (see Antolin and Van Doorsselaere (2013) for a description of the forward-modelling code). Note that we are not interested in the absolute values of the observables, but in the relative differences between the signatures of the wave and flow models. We modelled the Fe IX 171.073 Å and Fe XII 193.509 Å spectral lines, which correspond

[1] https://wiki.esat.kuleuven.be/FoMo.

to the dominant lines in the SDO/AIA 171 Å and 193 Å filters, respectively (Lemen *et al.*, 2012). Finally, the effect of the line-of-sight (LOS) angle was incorporated by integrating along different 'rays', as shown in Figure 2 by the dashed lines. A 0° LOS angle corresponds to a loop aligned with the LOS (*i.e.* the perturbations are travelling directly towards the observer), whereas a 90° LOS angle corresponds to a loop perpendicular to the LOS (*i.e.* there are no velocity perturbations aligned with the LOS). We denote the LOS angle as θ. For each of the numerical simulations, we present Doppler velocity, line width and the goodness-of-fit measure χ^2/χ_0^2 as a function of time. Here χ^2/χ_0^2 is a measure of how closely the Gaussian fit to the spectral line matches the corresponding Gaussian fit for the plasma at rest. Unless otherwise mentioned, a single-Gaussian fit to the spectral lines was used.

3. Initial-Value Results

In this section, we present initial-value results (*i.e.* there are no perturbations in the domain at $t = 0$) where the perturbations are driven at the bottom boundary and propagate into the domain. Hence, the system changes from initially being at rest to a system containing a wave or flow. The simulations are stopped before they reach the upper boundary, as can be seen in the single-strand example in Figure 2(a).

3.1. Single-Strand Wave and Flow

Figure 3 shows the temporal evolution of the Doppler velocity (top panels), the line width (middle panels), and the χ^2/χ_0^2 values (bottom panels) for the flow (black solid lines) and the wave (black dashed lines) for LOS angles of $\theta = 0°$, 15°, 45°, and 90°. The results shown in Figure 3 correspond to the Fe IX 171 Å line. Also overplotted are the summed density and temperature lines (blue and red lines). These are obtained by summing the density (temperature) perturbations along the LOS, relative to the equilibrium density (temperature) summed over a LOS of the same length ($\int_{\rm LOS} \rho \, {\rm d}l / \int_{\rm LOS} \rho_0 \, {\rm d}l$, where d$l$ represents the length along the line-of-sight).

For $\theta = 0°$, all the quantities show a steady change because these initial-value simulations do not reach a steady state before the end of the simulation: the volume of plasma supporting perturbations increases steadily during the simulations. We first examine the Doppler velocity. As expected for a (periodic) flow travelling towards the observer (and not in a steady state), the flow Doppler velocity constantly increases. However, a small, net blue-shift also builds up for the wave, even though the LOS-integrated quantities are averaged over a number of oscillations. This small blue-shift results from the fact that for a propagating slow wave, the velocity, density and temperature perturbations are in phase: because the Doppler velocities are weighted by the density, the integrated LOS values do not add up to zero as one might expect, because positive perturbations contribute more to the LOS average than the corresponding negative perturbations (see also Verwichte *et al.*, 2010). The line-widths (LW) similarly keep increasing, with the wave LW increasing more rapidly than the equivalent flow LW. In addition, the wave LWs oscillate with a double frequency. As pointed out by Verwichte *et al.* (2010), this is caused by the fact that a wave-like perturbation leads to excursions both to the blue and red side of the static line, and hence, the resulting total line profile (which consists of the static background plasma plus the perturbed component) will show additional line-broadening for both positive and negative values of the Doppler velocity perturbations, which in turn leads to a doubling of the LW oscillation frequency. This also explains why the wave LWs grow more rapidly than the corresponding flow LWs. Although

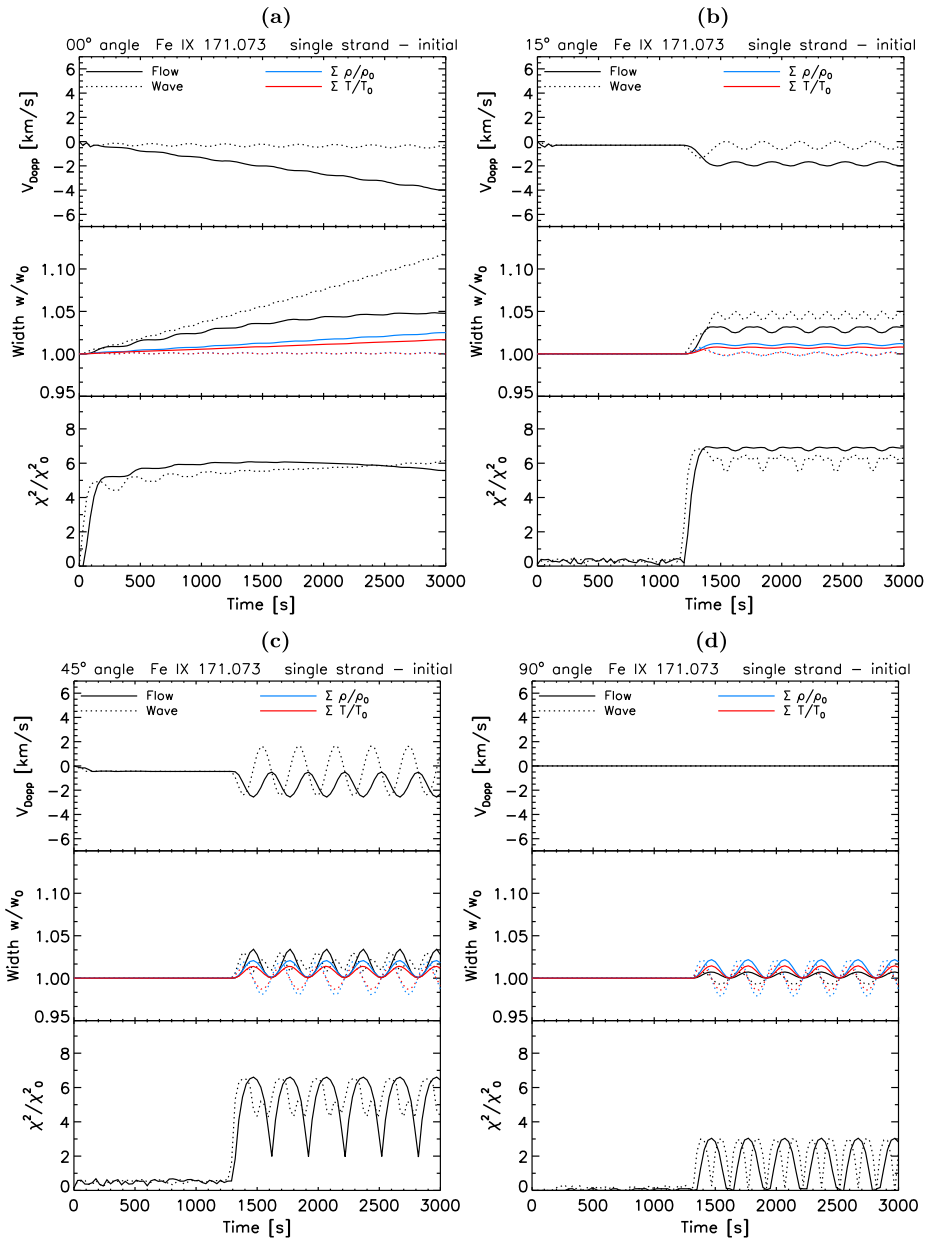

Figure 3 Time evolution (initial-value, single-strand case) of the Fe IX 171 Å Doppler velocity (top graphs in four panels), line widths (middle graphs) and the goodness-of-fit measure χ^2/χ_0^2 (bottom graphs) for tracing rays at angles of (a) 0°, (b) 15°, (c) 45°, and (d) 90°. The relative density (blue) and temperature (red) are overplotted for comparison. The results for the flow model are represented by the solid lines, those of the waves model by the dashed lines.

there are some other (physically) real differences in the Doppler velocity and LW evolution of the flow and wave model, these differences are only apparent in a direct comparison and hence cannot be used to observationally distinguish between the two models.

As can be seen from Figure 2(a), a steady state will be reached for LOS angles substantially greater than 0° before the end of the simulation. Even though this is an initial-value simulation, stopped before the perturbations reach the top boundary, for larger LOS angles a steady state is reached once the perturbations have travelled through the path of the ray. From that time onwards, the simulations are essentially similar to steady-state simulations because on average, no more material is added or perturbed. The larger the LOS angle, the quicker a steady state is reached as the perturbations cross a shorter ray path. The panels of Figure 3 for $\theta = 15°$ and $\theta = 45°$ indeed show that a steady state is reached quickly, as the Doppler velocity and LWs tend to constant values.

Finally, we consider the $\theta = 90°$ case. Here there is no velocity component aligned with the LOS and hence the Doppler velocities are zero for both the wave and flow model. The doubling of the wave LW frequency is now absent because the Doppler velocity perturbations are zero. The remaining changes in the wave LW are thermal LW changes, associated with the temperature and density perturbations. However, for $\theta = 90°$ the goodness-of-fit measure now shows a doubling in frequency for the wave model that is caused by the fact that the LW oscillates around its equilibrium value: both a maximum and a minimum in the wave LW corresponds to a maximum in χ^2. This is not the case for the flow, where the LW minima actually correspond to the equilibrium values: the perturbations in temperature and density for the flow are only ever positive relative to the equilibrium values.

3.2. Multistrand Wave and Flow

Figure 4 shows the results for the initial-value, multistrand simulation. Here five strands of different widths are considered, supporting oscillations with the same frequency, but slightly out of phase in time. Again the simulation is stopped before any of the perturbations reach the upper boundary. For $\theta = 0°$ we obtain exactly the same results as in the single-strand case described above because the LOS ray only crosses one of the strands. As before, we again see a doubling of the frequency for the wave LW, which is absent from the corresponding Doppler velocity perturbations. For inclined strands ($\theta = 15°$ and $\theta = 45°$) we see that the amplitude of the wave LW oscillations is no longer constant as a result of the complex addition of out-of-phase perturbations along the LOS. This is also obvious from the χ^2 values, which no longer show harmonic oscillations. The flow LWs, on the other hand, do appear to maintain their constant amplitudes, but have lost their sinusoidal shape. We also see some evidence of frequency doubling for the flow χ^2 measurements, although the effect is probably too small to be observable.

4. Harmonic Results

Although the initial-value results described in Section 3 are useful to understand the behaviour of the wave and flow observational signatures, in practise it is unlikely that observations will show initial-value perturbations (in other words, it is unlikely that we will observe the actual start of a train of perturbations). Hence, we also modelled steady-state, harmonic perturbations, *i.e.* the same perturbation (constant period) is travelling through the domain at all times. A representative snapshot taken from the multistrand simulations is shown in Figure 2(b). Because the numerical simulations we used are computationally cheap, reflec-

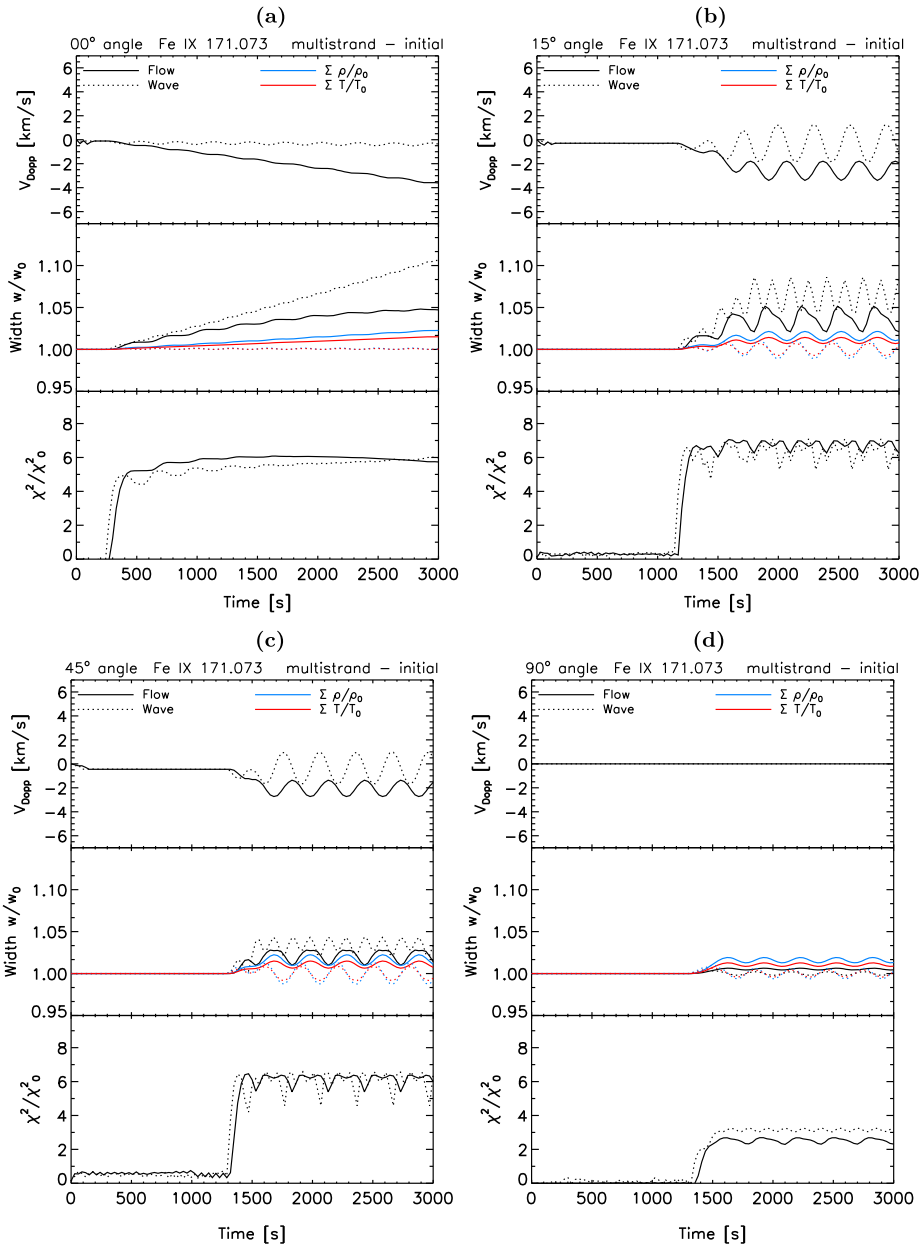

Figure 4 Time evolution (initial-value, multistrand case) of the Fe IX 171 Å Doppler velocity (top graphs in four panels), line widths (middle graphs), and χ^2/χ_0^2 (bottom graphs) for tracing rays at angles of (a) 0°, (b) 15°, (c) 45°, and (d) 90°.

tion from the top boundary is prevented by stopping the simulations before they reach the top boundary of a much larger box and then only considering the lower half of the box when forward-modelling the numerical results.

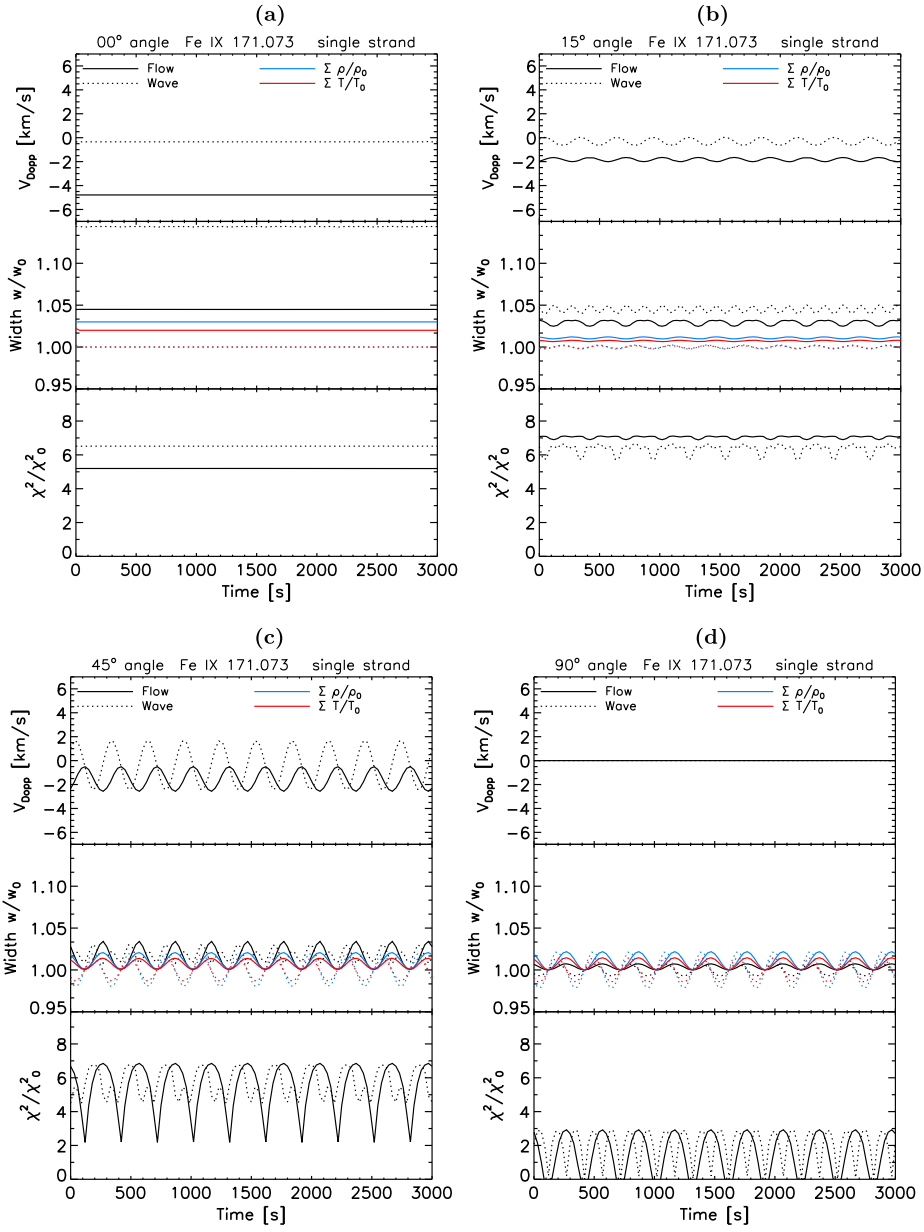

Figure 5 Time evolution (harmonic, single-strand case) of the Fe IX 171 Å Doppler velocity (top graphs in four panels), line widths (middle graphs), and χ^2/χ_0^2 (bottom graphs) for tracing rays at angles of (a) 0°, (b) 15°, (c) 45°, and (d) 90°.

4.1. Single-Strand Wave and Flow

As expected for a steady state, all quantities now reach (on average) constant values (see Figure 5). For $\theta = 0°$ there do not appear to be oscillations in any of the observable quan-

tities. There is a small, residual blue-shift for the wave, as discussed earlier, and a higher blue-shift for the flow, but these are both constant values. Observationally, constant values are difficult to measure directly because typical solar spectrometers lack absolute calibration and hence this difference is not a useful signature to distinguish between the periodic flow and wave models. There are no oscillations because there is an exact number of periods in the numerical domain in the vertical (y) direction (*i.e.* the direction of propagation). Hence, for a loop that is exactly aligned with the LOS, no oscillations would be visible in this case. However, this is a somewhat unlikely scenario, and in reality, it is more likely that a small residual oscillation would remain (in other words, it is unlikely that the oscillations would exactly cancel each other out along the LOS). We also note that our oscillations have a constant amplitude, whereas in reality, the amplitudes of the propagating disturbances are observed to decay as they travel along coronal loops.

As expected from the earlier results, the LW associated with the wave is higher than the flow LW, and this remains the case for shallow LOS angles. For example, the wave LWs are still larger than the flow ones for $\theta = 15°$, but this is no longer the case for $\theta = 45°$. For the intermediate angles ($\theta = 15°, 45°$) we again see the doubling of the frequency for the LWs associated with the wave. For $\theta = 90°$, the results are exactly the same as for the initial-value simulations, as expected (as the ray crosses the loop perpendicularly, an observer would see exactly the same signal as soon as the first full period of the perturbations has passed the ray in both cases).

4.2. Multistrand Wave and Flow

For the steady-state simulations, two different versions of the multistrand model were considered, namely one where all the phase differences between the individual strands are exactly the same (Figure 6 – referred to as the symmetric multistrand case), and one where they are different (Figure 7). Generally, the results are similar to those described earlier for the single-strand or the initial-value simulations. Note that the multistrand, initial-value simulation described in Section 3 also has symmetric phase differences, but they are slightly different from those used here. The position and width of the strands and the period of the perturbations were kept constant. These small differences in the phases of the initial-value simulations and the steady-state simulations have a small effect on the observational signatures, as can be seen from comparing Figures 4 and 6. However, none of these differences lead to observational signatures that could definitively distinguish between periodic flows or slow magneto-acoustic waves. Similarly, there are small differences between the symmetric, multistrand steady-state simulation and the non-symmetric case (compare Figures 6 and 7), but none that would be observationally distinguishable, apart from the frequency doubling in the wave LWs.

5. Fe XII Results

The results described so far all applied to observational signatures in the Fe IX 171 Å line. We now briefly examine the Fe XII 193 Å line. Overall, the results for Fe XII are very similar to the Fe IX results in the sense that there are of course difference between the wave and flow results, but none that could be used to observationally distinguish between the quasi-periodic flow or wave interpretations. However, in the multistrand, steady-state simulations, an interesting steepening of both the flow and wave Doppler velocities is found at intermediate LOS angles ($\theta = 15°$ and $45°$), as shown, for example, in Figure 8(a) for $\theta = 45°$. Excursions to

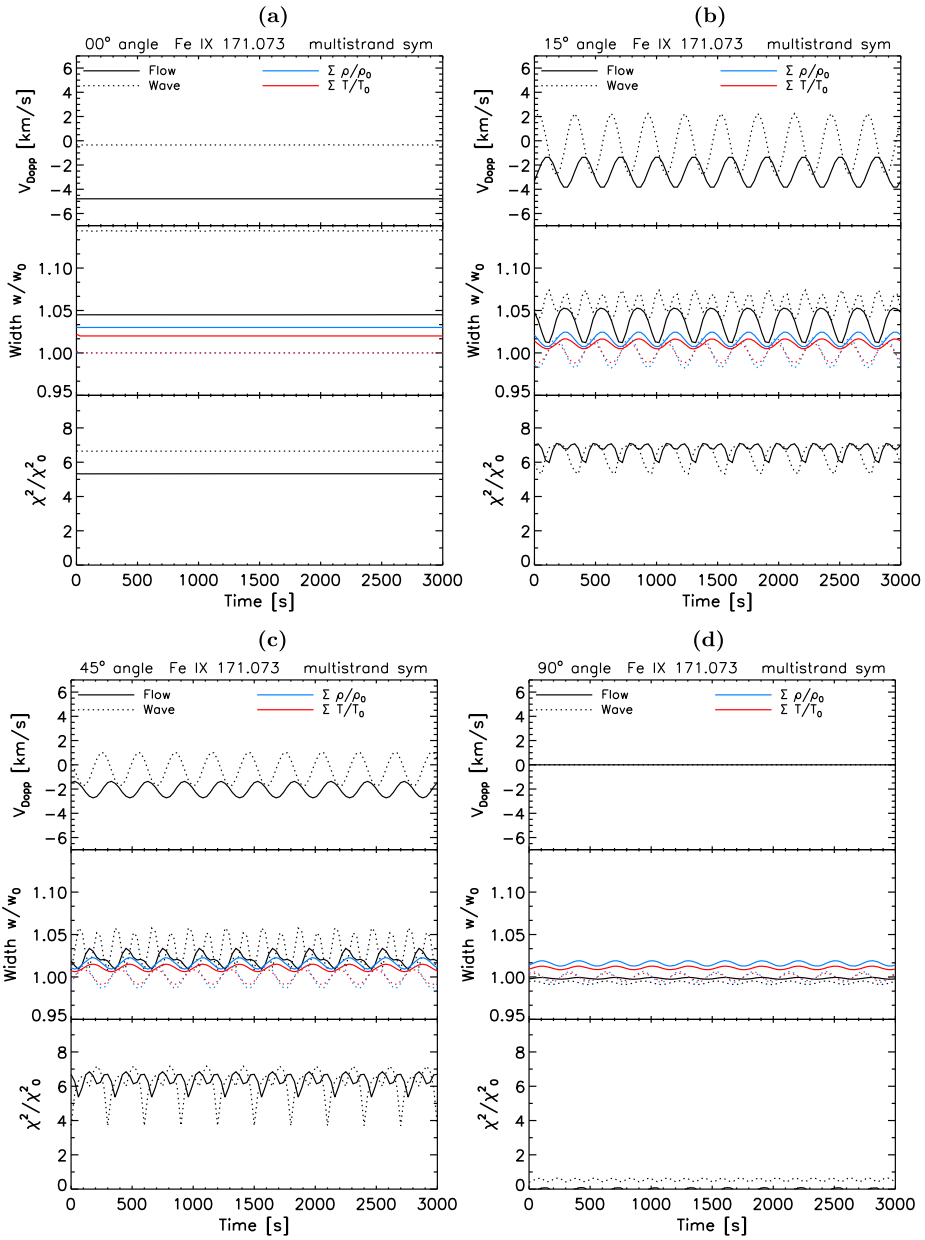

Figure 6 Time evolution (symmetric harmonic, multistrand case) of the Fe IX 171 Å Doppler velocity (top graphs in four panels), line widths (middle graphs), and χ^2/χ_0^2 (bottom graphs) for tracing rays at angles of (a) 0°, (b) 15°, (c) 45°, and (d) 90°.

the blue wing appear to occur very rapidly, giving the Doppler velocities a sawtooth appearance reminiscent of shocks, even though there are no actual (physical) shocks present in our numerical simulations. Exactly the same forward-modelled simulations in the Fe IX 171 Å line (Figure 7) show no apparent steepening at all, confirming that this is an entirely

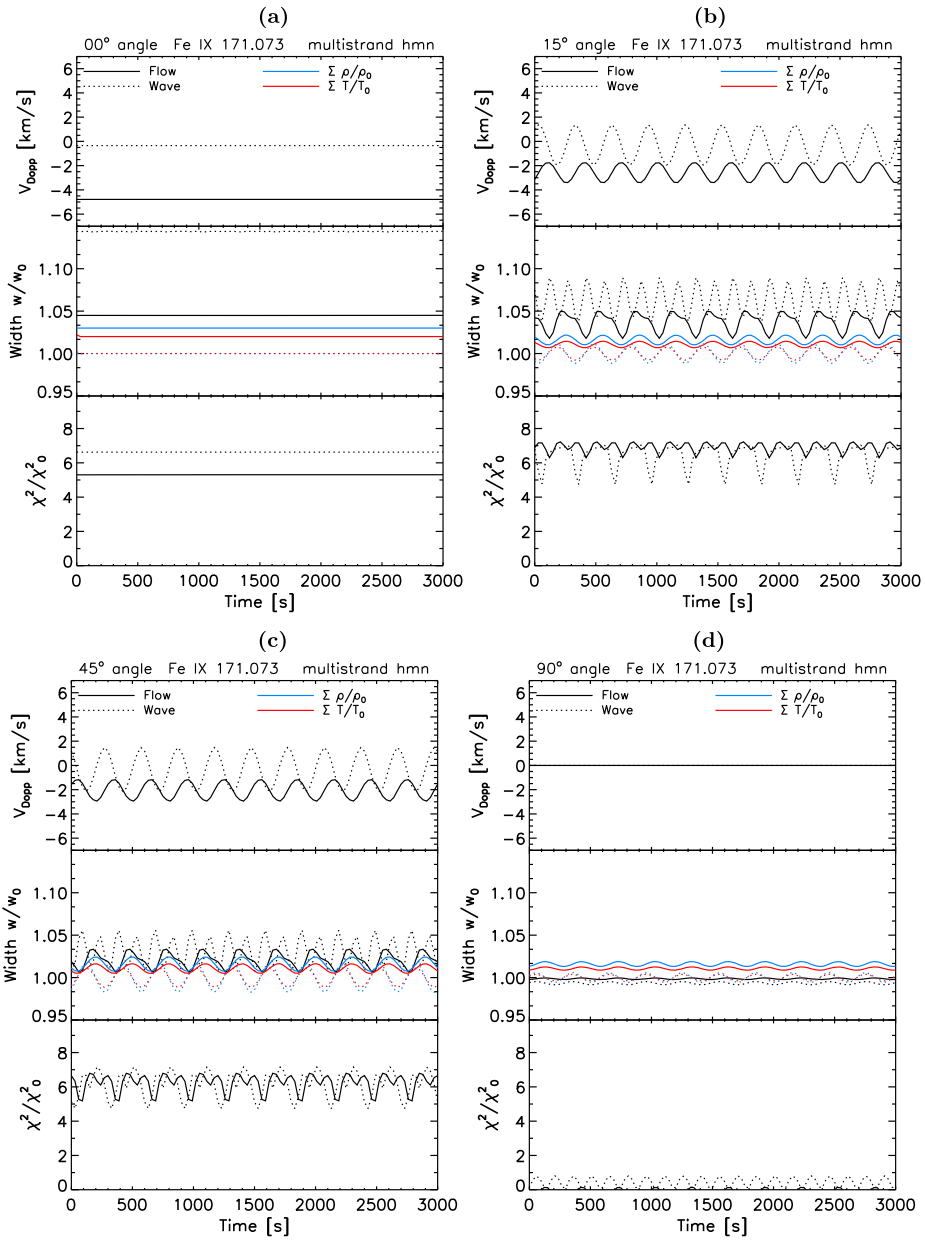

Figure 7 Time evolution (harmonic, multistrand case) of the Fe IX 171 Å Doppler velocity (top graphs in four panels), line widths (middle graphs), and χ^2/χ_0^2 (bottom graphs) for tracing rays at angles of (a) 0°, (b) 15°, (c) 45°, and (d) 90°.

observational effect. The sawtooth pattern can also be seen clearly in Figure 9, which shows a snapshot of the 193 Å emission for both the flow and the wave as a function of wavelength and distance perpendicular to the LOS.

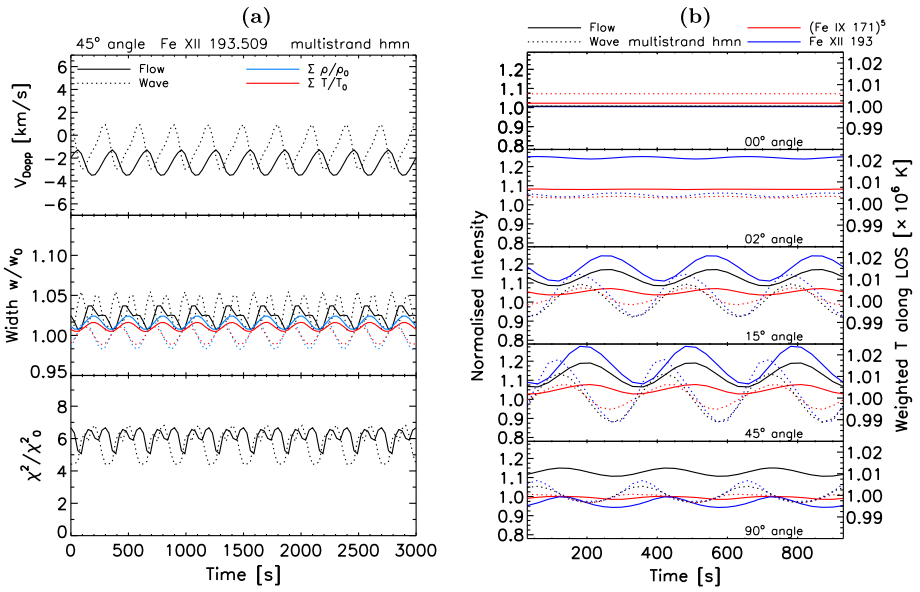

Figure 8 (a) Time evolution (harmonic, multistrand case) of the Fe XII 193 Å Doppler velocity (top panel), line widths (middle panel), and χ^2/χ_0^2 (bottom panel) for $\theta = 45°$. (b) The observed intensities along different LOS angles for Fe IX (red) and Fe XII (blue).

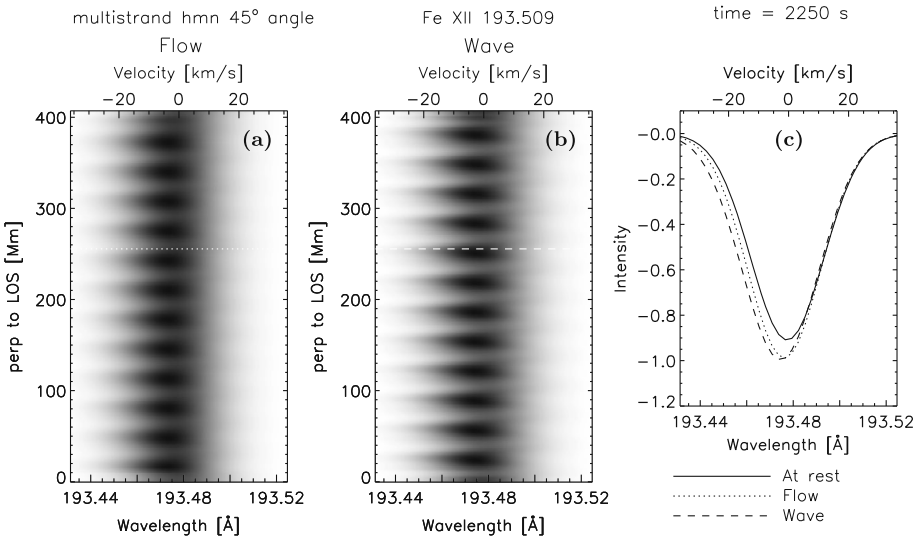

Figure 9 A (reverse-colour) snapshot (harmonic, multistrand, 45° at $t = 2250$ s) of the Fe XII spectral line as a function of distance perpendicular to the LOS for (a) the flow and (b) the wave. Panel (c) shows a horizontal cut through these snapshots.

Contributions along the LOS were weighted by $n^2 \times G(T, n)$, where $G(T, n)$ is the plasma response function (see *e.g.* Antolin and Van Doorsselaere, 2013). The difference between the 171 and 193 Å lines can be explained by examining the plasma response func-

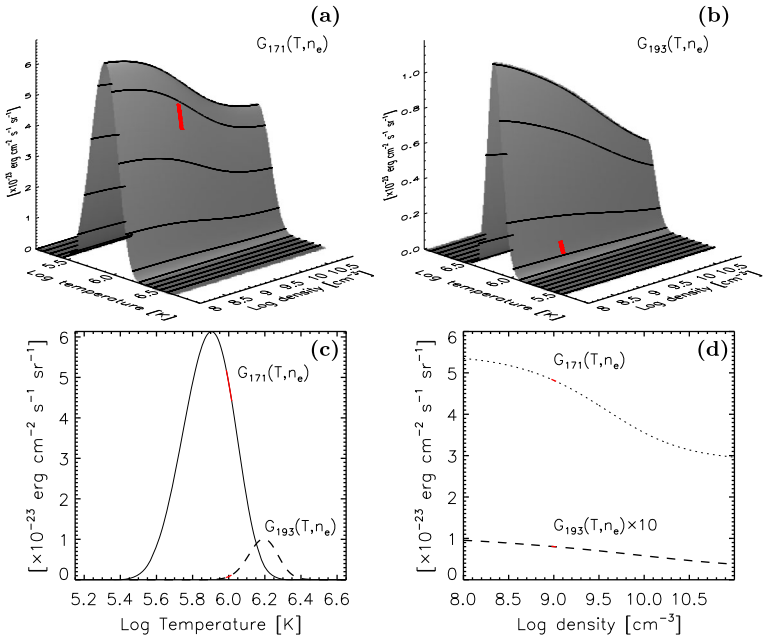

Figure 10 Surface plots of the emission function $G(T, n)$ for (a) Fe IX 171 Å and (b) Fe XII 193 Å as a function of (log) density and temperature. Note that the temperature axis has been reversed on the $G_{193}(T, n)$ surface plot. The bottom panels show slices through the domain at fixed density (c) and temperature (d). The relevant sections of G_{171} and G_{193} for the temperature and density ranges used in the models are indicated in red.

tion $G(T, n)$ in detail (Figure 10). Although this function depends on both temperature and density, for the range of temperatures and densities considered here, the dependence on density is very weak and can be ignored (see the cross-section as a function of density shown in Figure 10). The dependence of $G(T, n)$ on temperature is very different for the 171 and 193 Å lines (note that the temperature axis has been reversed on the $G_{193}(T, n)$ surface plot). For 171 Å, $G_{171}(T, n)$ decreases for increasing temperatures (because we are on the 'downhill' side of the $G_{171}(T, n)$ function for our chosen background temperature). For 193 Å, however, $G_{193}(T, n)$ increases with temperature. Maxima in temperature (and density) are in phase with the minima in the Doppler velocity (*i.e.* the highest blue-shifts). For 193 Å, an increase in temperature and density leads to a rapid increase in $n^2 \times G_{193}(T, n)$ (because n and $G_{193}(T, n)$ both increase), implying a larger weighting of blue-shifted regions along the LOS, leading to the asymmetric, sawtooth pattern in the Doppler velocities, where excursions to the blue side occur very rapidly. This rapid increase is absent from the 171 Å line because the increase in n is tempered by the simultaneous decrease in $G_{171}(T, n)$.

Figure 8(b) shows the actual intensity that would be observed for a range of LOS angles. For $\theta = 45°$ we can indeed see a similar steepening in the Fe XII 193 Å intensity, especially for the wave model (red dashed line). However, we also see that the corresponding intensity of the Fe IX 171 Å line shows a steepening in the opposite direction, although it is not as pronounced. The apparent "shocks" are more pronounced in the intensity perturbations associated with the wave model because the associated temperature and density perturbations are larger than in the flow model.

We emphasise again that this erratic "shock-like" profile is just an apparent effect, caused by the highly non-linear nature of the forward-modelling process (see also De Moortel and Bradshaw, 2008) and the particular width and alignment of the strands in this specific model and is in no way related to actual physical shocks.

6. Discussion

We aimed to use forward-modelling to investigate whether it is actually possible to (observationally) distinguish slow, propagating waves and (quasi-) periodic flows in a basic 2D model. Although there are of course a number of differences in the observational signatures described above, the majority are only identifiable when directly comparing the wave and flow models. However, in practise, a signature needs to be identifiable in isolation, and at least in the results presented above, no such signature is readily apparent (especially not when one considers that real observations would be less clear because of the additional effects of the background plasma, the plasma evolution (with height and time) and noise). The doubling of the frequency in the LW perturbations for the waves model could be a potential observational signature, but as discussed by Verwichte *et al.* (2010), the addition of a modest *steady* upflow component would cause the LW to oscillate again with the same period as the other parameters. Hence, these authors remarked that the absence of this frequency-doubling in the observed LWs cannot exclude the wave-interpretation of the PCDs because a steady upflow component cannot be excluded (owing to the lack of an absolute calibration of the spectrometers). We comment below in more detail on the LW frequency-doubling.

To try and avoid the need for a comparison between models, we considered the change with LOS angle of the averages of the Doppler velocities, line widths, and the χ^2/χ_0^2 values for the (single-strand) flow and wave model for the Fe IX 171 Å and Fe XII 193 Å lines in Figure 11. We also examined the ratio of these values in the two different spectral lines. A change of LOS angle could observationally be studied by tracking a loop (fan) system showing propagating coronal disturbances over a few days as it rotates across the solar disk, whereas ratios of the different quantities in different spectral lines could be obtained using data from *e.g. Hinode/EUV Imaging Spectrograph* (EIS; Culhane *et al.*, 2007) or the *Interface Region Imaging Spectrograph* (IRIS; De Pontieu *et al.*, 2014). The results were only shown for the single-strand model because those for the two multistrand models are very similar.

There are a few small differences between the two models. As expected, the Doppler velocities in the flow model remain higher (in absolute values) than for the wave model. The line widths, on the other hand, appear to be slightly larger for the wave model, but the difference would probably not be observable. We do see, however, that the LWs for the wave model change very rapidly for shallow LOS angles. In addition, the ratio of the Doppler velocities in the 171 and 193 Å lines is closer to one for the flow model than in the wave model. In other words, Doppler velocities derived from the two spectral lines are closer together for the flow model and farther apart for the waves model, again especially at shallow LOS angles.

In addition to examining the ratios in different spectral lines, one could also investigate the ratios between different amplitudes. Figure 12 shows the (logarithm of) ratios of the amplitudes of the line widths and the intensities ($\Delta w/\Delta I$ – red lines) and the line width amplitudes and the amplitudes of the Doppler perturbations ($\Delta w/\Delta v_{\mathrm{Dopp}}$ – blue lines) for the flow and wave models in the Fe IX (top panel) and Fe XII (bottom panel) spectral lines. In the bottom panel (Fe XII line), the two ratios are essentially the same for the wave model

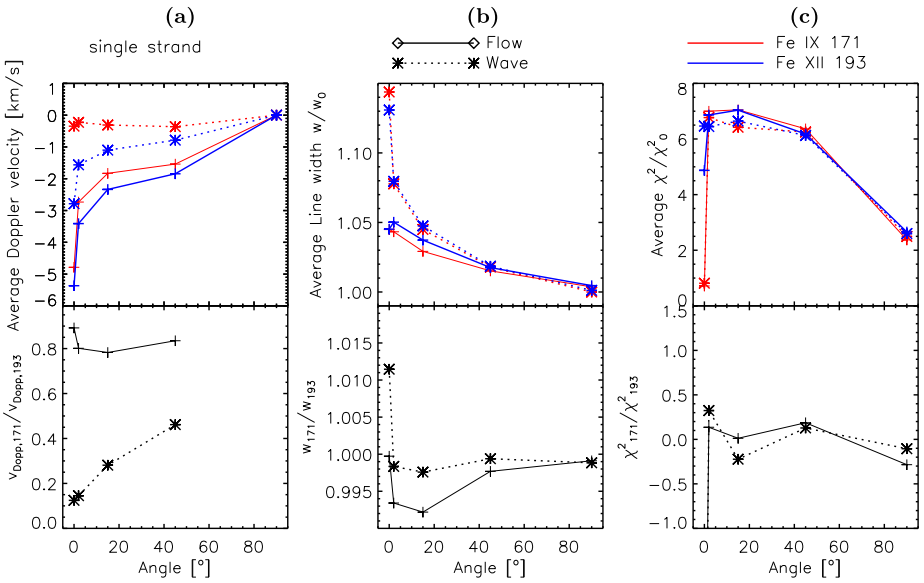

Figure 11 Averages of Doppler velocities (a), line widths (b), and χ^2/χ^2_0 (c) as a function of the LOS angle for the Fe IX (red) and Fe XII (blue) spectral lines individually (top panels). The ratio of these averages in the two spectral lines is shown in the bottom panels. As before, the results for the flow model are represented by solid lines, those of the waves model by the dashed lines.

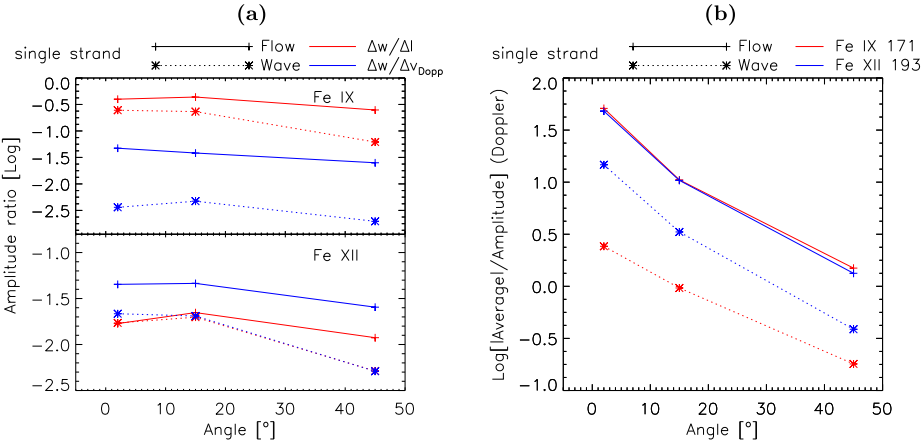

Figure 12 (a) Ratio of the amplitudes of the line widths and the intensities ($\Delta w/\Delta I$ – red lines) and the amplitudes of the line widths and the Doppler perturbations ($\Delta w/\Delta v_{\rm Dopp}$ – blue lines) as a function of the LOS angle, for Fe IX (top panel) and Fe XII (bottom panel). (b) Ratio of the average Doppler velocity and the amplitude of the Doppler velocities for Fe IX (red) and Fe XII (blue).

at every angle. However, there is a substantial difference between $\Delta w/\Delta I$ and $\Delta w/\Delta v_{\rm Dopp}$ in both spectral graphs for the flow model. These graphs suggest that $\Delta w/\Delta v_{\rm Dopp}$ might be used to distinguish between flows and waves. In Fe IX, the ratio $\Delta w/\Delta v_{\rm Dopp}$ is substantially higher for the flow than for the wave (by about an order of magnitude – compare the solid

and dashed blue lines in the top panel). For the flow, $\Delta w/\Delta v_{\mathrm{Dopp}}$ is of the order of $10^{-1.0}$ or $10^{-1.5}$ (that is, around $0.03-0.1$), whereas for the wave model, $\Delta w/\Delta v_{\mathrm{Dopp}} \approx 10^{-2.5} \approx 0.003$, which is considerably lower. In Fe XII, the flow and wave $\Delta w/\Delta v_{\mathrm{Dopp}}$ ratios are somewhat closer together, but are still at least a factor of 5 different. Such a large discrepancy may be directly observed, even without the other case as comparison (*i.e.* if one observes a high value for $\Delta w/\Delta v_{\mathrm{Dopp}}$, the flow scenario might be more likely.) However, the amplitude ratios do depend on the amplitude of the PCDs and properties of the equilibrium state, and the effects of those on the amplitude ratio have not been modelled in this article.

Perhaps the most straightforward usable signature to distinguish observationally is the simple fact that the average Doppler velocities of the wave model are close to zero. Although there is a net blue-shift in the wave model due to the in-phase relationship between the perturbed density and temperature and the velocities, it is generally small. This can also be seen in the top panel of Figure 2 of Verwichte *et al.* (2010), where the (averaged) wave Doppler velocity is plotted as a function of the wave amplitude. At least for linear perturbations ($v \lesssim 60\ \mathrm{km\,s^{-1}}$ in Figure 2 of Verwichte *et al.*, 2010), the average Doppler velocities are lower than the wave amplitudes. Hence, one way of distinguishing a slow wave from a periodic flow could be the interpretation that for a wave model, the amplitude of the Doppler velocity perturbations is larger than the average of the perturbations. Figure 12(b) shows the ratios of the absolute value of the mean of the Doppler velocities to the amplitude of the Doppler velocities. Here, we see that this ratio is indeed higher than one (higher than zero in the figure because the logarithm of the ratio has been plotted) for the flow for all LOS angles. In addition, the ratio is the same in both spectral lines for the flow model. Although we only show the results for the single-strand case, the same holds for the two multistrand cases. For the wave model, the ratio is lower than one (lower than zero in the logarithm plot) for Fe IX apart from at very shallow LOS angles. For Fe XII, however, the ratio is only lower than one for the wave for large LOS angles. However, for the single-strand and the multistrand cases, the ratio in Fe XII is substantially higher than in Fe IX at all LOS angles (as opposed to the equal ratios for the flow model), which could potentially be verified in spectral observations.

Theoretically, this difference between the average (or background) Doppler velocities and the perturbation amplitudes could be a feature that would allow distinguishing between the flow and wave interpretation. The reason for this is that a periodic flow can be decomposed into a steady background flow plus periodic perturbations oscillating around a zero mean, or, in other words, a slow propagating wave, as was pointed out in Section 2. Equation (1) clearly shows that the only difference between the flow and wave model is exactly this background value; the periodic flow can be reduced to a slow wave by subtracting the mean of the perturbations (*i.e.* the steady background value). However, observationally, the difficulty would lie in determining the absolute value of the background: in practise, background values are often subtracted and only the relative amplitudes are studied, which would eliminate this difference between the wave and flow models. Note also that this interpretation implies that the suggestion by Verwichte *et al.* (2010) to add a modest upflow to the wave model to avoid the frequency-doubling in the line widths could essentially transform their wave model into a periodic upflow model (depending on the size of the additional steady upflow component). In other words, if the frequency-doubling of the line widths is not observed, the interpretation in terms of a quasi-periodic upflow model might be more appropriate. In addition, this interpretation implies the existence of an intermediate regime, where the average (background) Doppler velocity and the perturbation amplitudes are similar in size.

In this study, the periodic flow model we have studied can be decomposed into a steady background flow and a wave of the same amplitude because of our particular choice of

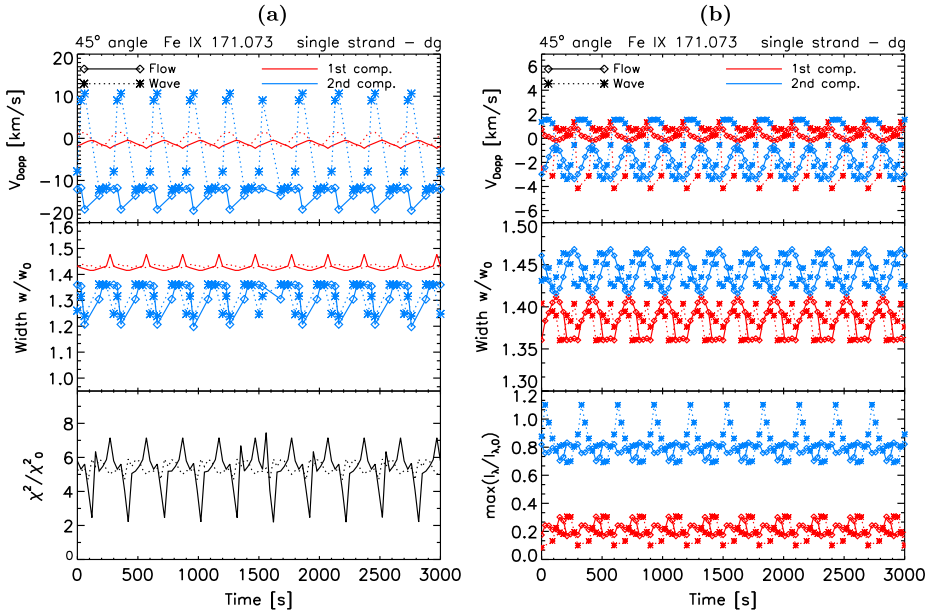

Figure 13 Time evolution of the harmonic, single-strand case based on double-Gaussian fits (first component in red, second component in blue). Results in panel (a) are obtained without providing an initial guess for the fitting routine, while panel (b) shows results using the single-Gaussian fit as an initial guess (see text for more details). Note that the bottom panel of (b) shows the perturbed intensities and not the goodness-of-fit measure.

boundary driving. Of course, various combinations of the background flow amplitude and the perturbation amplitude would lead to different observational signatures, but the results presented here show that there will most likely only be relative differences between a wave and periodic flow interpretation rather than (observationally useful) absolute differences.

It is important to point out that the results presented here were obtained by fitting a single Gaussian to the spectral data. This is a crucial difference from, for example, observational results presented by De Pontieu *et al.* (2009) or De Pontieu and McIntosh (2010), who argued that a double-Gaussian fit should be used to account for the persistent red-blue asymmetry present in the spectral data (showing an excess in the blue wing when using a single-Gaussian fit). In Figure 13 we present two examples of a double-Gaussian fit for the steady, single-strand model at $\theta = 45°$. Figure 13(a) is obtained without giving an initial guess to the fitting routine. Figure 13(b) uses the maximum value, the centre position, and the width of the line at rest as an initial guess for the first component and the centre position and line width of the single-Gaussian fit as an initial guess for the second component. Figure 13(a) shows a nearly static first component (red lines) and a secondary component that still oscillates around near-zero for the wave model, but around a much higher (blue-shifted) value for the flow. In fact, for the flow, the secondary component appears to significantly overestimate the velocity amplitudes, oscillating around a value of about 15 km s^{-1}, whereas the model velocities had maximum values just below 10 km s^{-1} (see Figure 1(a)). However, one has to keep in mind that the single-Gaussian fit significantly *underestimated* the velocity values (see Figure 5), more so than the overestimate associated with this double-Gaussian fit. Hence, one could argue that the double-Gaussian fit is actually the better result. In addition, the (small) oscillation in the first component is out of phase with the secondary component

for the flow model. When an initial guess is provided (Figure 13(b)), the flow still shows a first component with only small oscillations around zero and a (now underestimated) blue-shifted second component (again out of phase with the first component). However, the wave model (dashed lines) shows a very different behaviour: the first and second components are both oscillating, with similar amplitudes, but out of phase. The corresponding LWs show a relatively regular behaviour for the flow model, with the first and second components oscillating out of phase, and again show some evidence of frequency doubling for the wave model.

From the first double-Gaussian example, we can see that for the wave model, the first and secondary component would both show a similar mean (close to zero in our simple model), whereas for the periodic flows, the mean of the secondary component differs substantially from the static (background) component. This essentially leads to the same conclusion as the single-Gaussian fits presented in this article: quasi-periodic flows are characterised by perturbed Doppler velocities that have amplitudes smaller than their mean, whereas for the slow, propagating waves, the perturbation amplitudes are larger than the mean (which will be close to zero). However, the second double-Gaussian fit shows worryingly different results, indicating the fitting is very sensitive to the initial guess provided, and this could also be the case for low signal-to-noise (noisy) observations. Hence, one would need to provide appropriately (physically) justified initial guesses for the fitting routine, but it is hard to see how this can be done without pre-determining the physical model. The double-Gaussian fitting used by De Pontieu and McIntosh (2010) is motivated not just by the persistent nature of the red-blue asymmetries in the single-Gaussian fit, but, more importantly, by the fact that these single-Gaussian R-B asymmetries (which can be thought of as a proxy for the goodness-of-fit χ^2) are not uniform, but show (physical) structuring (as can be seen for example in Figure 1(e) of De Pontieu and McIntosh, 2010). Such physical structuring in a goodness-of-fit measure indicates that essential physics is lacking in the (single-Gaussian fit) model and hence that a more complex model, such as the double-Gaussian fit used by these authors, is needed. The values of the R-B asymmetries in the single-Gaussian fit are used as the initial guess for the secondary component of the double-Gaussian fit, which seems an appropriate initial guess. However, it is worth noting here that fixing the centre position of the secondary component relatively far out in the blue wing in this way almost automatically results in (small) period Doppler shifts on top of a large, persistent blue-shift, or, in other words, the periodic flow model.

We also point out that the relatively small size of our numerical domain is likely to affect our results as well. In our simple model, the line profiles are dominated by the flow or wave components rather than by the (surrounding) plasma at rest, which potentially makes them more sensitive to the initial guess. In reality, it is likely the reverse, with the plasma at rest along the LOS dominating the emission and not the perturbed plasma (flow or wave), which might lead to a more stable fitting of (at least) the primary component.

Finally, we emphasise how different some of the observational signatures can look from the actual underlying theoretical model. This was nicely illustrated by the apparent "shocks" in the Fe XII 193 Å lines along one particular LOS, when the velocity perturbations in our simulations are relatively small and show no signs of shocks. In this article, we only varied one of the parameters of the multistrand model, namely the phase difference between the oscillations in neighbouring strands. Even this small change leads to noticeable changes in the observational signatures. In reality, there would of course be far more variations possible; the width of the strands, the number of the strands, the amplitude and periods of the perturbations could all be varied, as well as the background temperature and density of the strands.

7. Conclusions

As was already apparent from the inconclusive observational debate on the nature of the observed propagating disturbances (PCDs), finding unique and robust observational signatures to distinguish the propagating, slow magneto-acoustic wave model and the quasi-periodic upflow interpretation is highly non-trivial. Even the basic model presented here clearly shows that observational signatures are highly model-dependent, and distinguishing between slow, propagating waves and periodic flows might simply not be possible.

Possible observational signatures that might allow distinguishing the periodic upflow and slow propagating wave models are:

- the average line widths for the wave model vary rapidly as a function of LOS angle for shallow LOS angles;
- the ratio of the line width amplitudes to the Doppler velocity amplitudes ($\Delta w/\Delta v_{\rm Dopp}$) for flows is relatively high, especially in the Fe IX line;
- the ratio of the mean to the amplitude of the Doppler perturbations is higher than one for the flow model and in our upflow model was the same in the Fe IX and Fe XII spectral lines.

This last property appears to be the most robust signature. Linked to this is the absence of frequency-doubling in the observed line widths, which (as suggested by Verwichte *et al.*, 2010) could indicate the presence of a steady upflow component along the LOS and hence, in this interpretation, would make a flow model more appropriate. We do caution, however, that the switch (*i.e.* the critical mean/amplitude ratio) between the flow and wave model suggested here might be model dependent and hence a more comprehensive parameter-space investigation would be useful to confirm this. We also recall that the results obtained in this study are based on single-Gaussian fits to the spectral lines.

The most likely scenario able to account for the observational results (and discrepancies) appears to be the dual model, where upflows at the very base of the coronal loops generate a slow magneto-acoustic wave that travels along the coronal loop. This dual model accommodates the differences between the spectral observations (which are often situated near the loop footpoint and find slightly lower speeds – *i.e.* they are mainly seeing the flow component of the dual model) and the (coronal) imaging observations (observing the more extended coronal structures showing PCDs travelling at constants speeds of about the local sound speed, *i.e.* the wave component of the dual model).

Acknowledgements IDM acknowledges support of a Royal Society University Research Fellowship and a KU Leuven Research Council senior research fellowship (SF/12/008).The research leading to these results has also received funding from the European Commission Seventh Framework Programme (FP7/2007-2013) under the grant agreement SOLSPANET (project No. 269299, www.solspanet.eu/solspanet). TVD has been sponsored by an Odysseus grant of the FWO Vlaanderen. The research was performed in the context of the IAP P7/08 CHARM (Belspo) and the GOA-2015-014 (KU Leuven). TVD acknowledges the funding from the FP7 ERG grant with number 276808. The authors would like to thank S.W. McIntosh for helpful discussions.

References

Antolin, P., Van Doorsselaere, T.: 2013, Line-of-sight geometrical and instrumental resolution effects on intensity perturbations by sausage modes. *Astron. Astrophys.* **555**, A74. DOI. ADS.

Arber, T.D., Longbottom, A.W., Gerrard, C.L., Milne, A.M.: 2001, A staggered grid, Lagrangian–Eulerian remap code for 3-D MHD simulations. *J. Comput. Phys.* **171**, 151. DOI. ADS.

Banerjee, D., Gupta, G.R., Teriaca, L.: 2011, Propagating MHD waves in coronal holes. *Space Sci. Rev.* **158**, 267. DOI. ADS.

Banerjee, D., O'Shea, E., Doyle, J.G.: 2000, Long-period oscillations in polar plumes as observed by cds on soho. *Solar Phys.* **196**, 63. DOI. ADS.

Berghmans, D., Clette, F.: 1999, Active region EUV transient brightenings – First results by EIT of SOHO JOP80. *Solar Phys.* **186**, 207. DOI. ADS.

Bryans, P., Young, P.R., Doschek, G.A.: 2010, Multiple component outflows in an active region observed with the EUV imaging spectrometer on Hinode. *Astrophys. J.* **715**, 1012. DOI. ADS.

Culhane, J.L., Harra, L.K., James, A.M., Al-Janabi, K., Bradley, L.J., Chaudry, R.A., Rees, K., Tandy, J.A., Thomas, P., Whillock, M.C.R., Winter, B., Doschek, G.A., Korendyke, C.M., Brown, C.M., Myers, S., Mariska, J., Seely, J., Lang, J., Kent, B.J., Shaughnessy, B.M., Young, P.R., Simnett, G.M., Castelli, C.M., Mahmoud, S., Mapson-Menard, H., Probyn, B.J., Thomas, R.J., Davila, J., Dere, K., Windt, D., Shea, J., Hagood, R., Moye, R., Hara, H., Watanabe, T., Matsuzaki, K., Kosugi, T., Hansteen, V., Wikstol, Ø.: 2007, The EUV Imaging Spectrometer for Hinode. *Solar Phys.* **243**, 19. DOI. ADS.

De Moortel, I.: 2009, Longitudinal waves in coronal loops. *Space Sci. Rev.* **149**, 65. DOI. ADS.

De Moortel, I., Bradshaw, S.J.: 2008, Forward modelling of coronal intensity perturbations. *Solar Phys.* **252**, 101. DOI. ADS.

De Moortel, I., Hood, A.W.: 2003, The damping of slow MHD waves in solar coronal magnetic fields. *Astron. Astrophys.* **408**, 755. DOI. ADS.

De Moortel, I., Hood, A.W.: 2004, The damping of slow MHD waves in solar coronal magnetic fields. II. The effect of gravitational stratification and field line divergence. *Astron. Astrophys.* **415**, 705. DOI. ADS.

De Moortel, I., Ireland, J., Walsh, R.W.: 2000, Observation of oscillations in coronal loops. *Astron. Astrophys.* **355**, L23. ADS.

De Moortel, I., Nakariakov, V.M.: 2012, Magnetohydrodynamic waves and coronal seismology: An overview of recent results. *Phil. Trans. Roy. Soc. London A* **370**, 3193. DOI. ADS.

De Moortel, I., Hood, A.W., Ireland, J., Walsh, R.W.: 2002a, Longitudinal intensity oscillations in coronal loops observed with TRACE II. Discussion of measured parameters. *Solar Phys.* **209**, 89. DOI. ADS.

De Moortel, I., Ireland, J., Walsh, R.W., Hood, A.W.: 2002b, Longitudinal intensity oscillations in coronal loops observed with TRACE I. Overview of measured parameters. *Solar Phys.* **209**, 61. DOI. ADS.

De Pontieu, B., McIntosh, S.W.: 2010, Quasi-periodic propagating signals in the solar corona: The signature of magnetoacoustic waves or high-velocity upflows? *Astrophys. J.* **722**, 1013. DOI. ADS.

De Pontieu, B., McIntosh, S.W., Hansteen, V.H., Schrijver, C.J.: 2009, Observing the roots of solar coronal heating in the chromosphere. *Astrophys. J. Lett.* **701**, L1. DOI. ADS.

De Pontieu, B., McIntosh, S.W., Carlsson, M., Hansteen, V.H., Tarbell, T.D., Boerner, P., Martinez-Sykora, J., Schrijver, C.J., Title, A.M.: 2011, The origins of hot plasma in the solar corona. *Science* **331**. DOI. ADS.

De Pontieu, B., Title, A.M., Lemen, J.R., Kushner, G.D., Akin, D.J., Allard, B., Berger, T., Boerner, P., Cheung, M., Chou, C., Drake, J.F., Duncan, D.W., Freeland, S., Heyman, G.F., Hoffman, C., Hurlburt, N.E., Lindgren, R.W., Mathur, D., Rehse, R., Sabolish, D., Seguin, R., Schrijver, C.J., Tarbell, T.D., Wülser, J.-P., Wolfson, C.J., Yanari, C., Mudge, J., Nguyen-Phuc, N., Timmons, R., van Bezooijen, R., Weingrod, I., Brookner, R., Butcher, G., Dougherty, B., Eder, J., Knagenhjelm, V., Larsen, S., Mansir, D., Phan, L., Boyle, P., Cheimets, P.N., DeLuca, E.E., Golub, L., Gates, R., Hertz, E., McKillop, S., Park, S., Perry, T., Podgorski, W.A., Reeves, K., Saar, S., Testa, P., Tian, H., Weber, M., Dunn, C., Eccles, S., Jaeggli, S.A., Kankelborg, C.C., Mashburn, K., Pust, N., Springer, L., Carvalho, R., Kleint, L., Marmie, J., Mazmanian, E., Pereira, T.M.D., Sawyer, S., Strong, J., Worden, S.P., Carlsson, M., Hansteen, V.H., Leenaarts, J., Wiesmann, M., Aloise, J., Chu, K.-C., Bush, R.I., Scherrer, P.H., Brekke, P., Martinez-Sykora, J., Lites, B.W., McIntosh, S.W., Uitenbroek, H., Okamoto, T.J., Gummin, M.A., Auker, G., Jerram, P., Pool, P., Waltham, N.: 2014, The Interface Region Imaging Spectrograph (IRIS). *Solar Phys.* **289**, 2733. DOI. ADS.

DeForest, C.E., Gurman, J.B.: 1998, Observation of quasi-periodic compressive waves in solar polar plumes. *Astrophys. J. Lett.* **501**, L217. DOI. ADS.

Del Zanna, G.: 2008, Flows in active region loops observed by hinode EIS. *Astron. Astrophys.* **481**, L49. DOI. ADS.

Doschek, G.A., Warren, H.P., Mariska, J.T., Muglach, K., Culhane, J.L., Hara, H., Watanabe, T.: 2008, Flows and nonthermal velocities in solar active regions observed with the EUV Imaging Spectrometer on Hinode: A tracer of active region sources of heliospheric magnetic fields? *Astrophys. J.* **686**, 1362. DOI. ADS.

Hara, H., Watanabe, T., Harra, L.K., Culhane, J.L., Young, P.R., Mariska, J.T., Doschek, G.A.: 2008, Coronal plasma motions near footpoints of active region loops revealed from spectroscopic observations with Hinode EIS. *Astrophys. J.* **678**, L67. DOI. ADS.

Harra, L.K., Sakao, T., Mandrini, C.H., Hara, H., Imada, S., Young, P.R., van Driel-Gesztelyi, L., Baker, D.: 2008, Outflows at the edges of active regions: Contribution to solar wind formation? *Astrophys. J.* **676**, L147. DOI. ADS.

He, J.-S., Marsch, E., Tu, C.-Y., Guo, L.-J., Tian, H.: 2010, Intermittent outflows at the edge of an active region – A possible source of the solar wind? *Astron. Astrophys.* **516**, A14. DOI. ADS.

Lemen, J.R., Title, A.M., Akin, D.J., Boerner, P.F., Chou, C., Drake, J.F., Duncan, D.W., Edwards, C.G., Friedlaender, F.M., Heyman, G.F., Hurlburt, N.E., Katz, N.L., Kushner, G.D., Levay, M., Lindgren, R.W., Mathur, D.P., McFeaters, E.L., Mitchell, S., Rehse, R.A., Schrijver, C.J., Springer, L.A., Stern, R.A., Tarbell, T.D., Wuelser, J.-P., Wolfson, C.J., Yanari, C., Bookbinder, J.A., Cheimets, P.N., Caldwell, D., Deluca, E.E., Gates, R., Golub, L., Park, S., Podgorski, W.A., Bush, R.I., Scherrer, P.H., Gummin, M.A., Smith, P., Auker, G., Jerram, P., Pool, P., Soufli, R., Windt, D.L., Beardsley, S., Clapp, M., Lang, J., Waltham, N.: 2012, The Atmospheric Imaging Assembly (AIA) on the Solar Dynamics Observatory (SDO). *Solar Phys.* **275**, 17. DOI. ADS.

Marsh, M.S., Walsh, R.W.: 2009, Using HINODE/Extreme-ultraviolet Imaging Spectrometer to confirm a seismologically inferred coronal temperature. *Astrophys. J. Lett.* **706**, L76. DOI. ADS.

Marsh, M.S., Walsh, R.W., Plunkett, S.: 2009, Three-dimensional coronal slow modes: Toward three-dimensional seismology. *Astrophys. J.* **697**, 1674. DOI. ADS.

McIntosh, S.W.: 2012, Recent observations of plasma and Alfvénic wave energy injection at the base of the fast solar wind. *Space Sci. Rev.* **172**, 69. DOI. ADS.

McIntosh, S.W., De Pontieu, B.: 2009a, High-speed transition region and coronal upflows in the quiet Sun. *Astrophys. J.* **707**, 524. DOI. ADS.

McIntosh, S.W., De Pontieu, B.: 2009b, Observing episodic coronal heating events rooted in chromospheric activity. *Astrophys. J.* **706**, L80. DOI. ADS.

McIntosh, S.W., Innes, D.E., de Pontieu, B., Leamon, R.J.: 2010, STEREO observations of quasi-periodically driven high velocity outflows in polar plumes. *Astron. Astrophys.* **510**, L2. DOI. ADS.

McIntosh, S.W., Tian, H., Sechler, M., De Pontieu, B.: 2012, On the Doppler velocity of emission line profiles formed in the "Coronal contraflow" that is the chromosphere-corona mass cycle. *Astrophys. J.* **749**, 60. DOI. ADS.

Nishizuka, N., Hara, H.: 2011, Spectroscopic observations of continuous outflows and propagating waves from NOAA 10942 with Extreme ultraviolet Imaging Spectrometer/Hinode. *Astrophys. J. Lett.* **737**, L43. DOI. ADS.

Ofman, L., Nakariakov, V.M., Sehgal, N.: 2000, Dissipation of slow magnetosonic waves in coronal plumes. *Astrophys. J.* **533**, 1071. DOI. ADS.

Ofman, L., Wang, T.J., Davila, J.M.: 2012, Slow magnetosonic waves and fast flows in active region loops. *Astrophys. J.* **754**, 111. DOI. ADS.

Ofman, L., Romoli, M., Poletto, G., Noci, G., Kohl, J.L.: 1997, Ultraviolet coronagraph spectrometer observations of density fluctuations in the solar wind. *Astrophys. J.* **491**, L111. DOI. ADS.

Owen, N.R., De Moortel, I., Hood, A.W.: 2009, Forward modelling to determine the observational signatures of propagating slow waves for TRACE, SoHO/CDS, and Hinode/EIS. *Astron. Astrophys.* **494**, 339. DOI. ADS.

Peter, H.: 2010, Asymmetries of solar coronal extreme ultraviolet emission lines. *Astron. Astrophys.* **521**, A51. DOI. ADS.

Sakao, T., Kano, R., Narukage, N., Kotoku, J., Bando, T., DeLuca, E.E., Lundquist, L.L., Tsuneta, S., Harra, L.K., Katsukawa, Y., Kubo, M., Hara, H., Matsuzaki, K., Shimojo, M., Bookbinder, J.A., Golub, L., Korreck, K.E., Su, Y., Shibasaki, K., Shimizu, T., Nakatani, I.: 2007, Continuous plasma outflows from the edge of a solar active region as a possible source of solar wind. *Science* **318**. DOI. ADS.

Schrijver, C.J., Title, A.M., Berger, T.E., Fletcher, L., Hurlburt, N.E., Nightingale, R.W., Shine, R.A., Tarbell, T.D., Wolfson, J., Golub, L., Bookbinder, J.A., Deluca, E.E., McMullen, R.A., Warren, H.P., Kankelborg, C.C., Handy, B.N., de Pontieu, B.: 1999, A new view of the solar outer atmosphere by the transition region and coronal explorer. *Solar Phys.* **187**, 261. DOI. ADS.

Tian, H., McIntosh, S.W., De Pontieu, B.: 2011, The spectroscopic signature of quasi-periodic upflows in active region timeseries. *Astrophys. J.* **727**, L37. DOI. ADS.

Ugarte-Urra, I., Warren, H.P.: 2011, Temporal variability of active region outflows. *Astrophys. J.* **730**, 37. DOI. ADS.

Van Doorsselaere, T., Wardle, N., Del Zanna, G., Jansari, K., Verwichte, E., Nakariakov, V.M.: 2011, The first measurement of the adiabatic index in the solar corona using time-dependent spectroscopy of Hinode/EIS observations. *Astrophys. J. Lett.* **727**, L32. DOI. ADS.

Verwichte, E., Marsh, M., Foullon, C., Van Doorsselaere, T., De Moortel, I., Hood, A.W., Nakariakov, V.M.: 2010, Periodic spectral line asymmetries in solar coronal structures from slow magnetoacoustic waves. *Astrophys. J. Lett.* **724**, L194. DOI. ADS.

Wang, T., Ofman, L., Davila, J.M.: 2012, Spectroscopic diagnosis of propagating disturbances in coronal loops: Waves or flows? In: Golub, L., De Moortel, I., Shimizu, T. (eds.) *Fifth Hinode Science Meeting*, *ASP Conf. Ser.* **456**, 91. ADS.

Wang, T., Ofman, L., Davila, J.M.: 2013, Three-dimensional magnetohydrodynamic modeling of propagating disturbances in fan-like coronal loops. *Astrophys. J. Lett.* **775**, L23. DOI. ADS.

Wang, T.J., Ofman, L., Davila, J.M., Mariska, J.T.: 2009, Hinode/EIS observations of propagating low-frequency slow magnetoacoustic waves in fan-like coronal loops. *Astron. Astrophys.* **503**, L25. DOI. ADS.

Warren, H.P., Ugarte-Urra, I., Young, P.R., Stenborg, G.: 2011, The temperature dependence of solar active region outflows. *Astrophys. J.* **727**, 58. DOI. ADS.

Winebarger, A.R., Warren, H., van Ballegooijen, A., DeLuca, E.E., Golub, L.: 2002, Steady flows detected in extreme-ultraviolet loops. *Astrophys. J.* **567**, L89. DOI. ADS.